Electronic Supplementary Material (ESI) for Journal of Materials Chemistry A.
This journal is © The Royal Society of Chemistry 2021

Supporting Information

A defect-driven atomically dispersed Fe-N-C electrocatalyst for bifunctional oxygen electrocatalytic activity in Zn-air battery

Jie Zhang[a], Jinwei Chen[a,b,*], Yan Luo[a], Yihan Chen[a], Yingjian Luo[a], Chenyang Zhang[a], Yali Xue[a], Honggang Liu[a], Gang Wang[a,b], Ruilin Wang [a,b,*]

[a] College of Materials Science and Engineering, Sichuan University, Chengdu 610065, China.

[b] Engineering Research Center of Alternative Energy Materials & Devices, Ministry of Education, Chengdu, 610065, China

---

*Corresponding authors at: College of Materials Science and Engineering, Sichuan University, No.24 South Section 1, Yihuan Road, Chengdu 610065, P.R. China. Tel: +86-028-85418786; Fax: +86-028-85418786; E-mails address: jwchen@scu.edu.cn (J.W. Chen) and rl.wang@scu.edu.cn (R.L. Wang)

Theoretical simulation

DFT calculations were performed in the Vienna ab initio simulation package (VASP). A spin-polarized GGA PBE functional, all-electron plane-wave basis sets with an energy cutoff of 520 eV, and a projector augmented wave (PAW) method were adopted. Graphene is simulated using a surface model of p (4 × 4) unit cell periodicity. A (3 × 3 × 1) Monkhorst-Pack mesh was used for the Brillouin-zone integrations to be sampled. The conjugate gradient algorithm was used in the optimization. The convergence threshold was set 1*10-4 eV in total energy and 0.05 eV/Å in force on each atom.

The free energy change (ΔG) for adsorptions were determined as follows:

$$\Delta G = E_{total} - E_{sur} + \Delta E_{ZPE} - T\Delta S$$

where E_{total} is the total energy for the adsorption state, E_{sur} is the energy of pure surface, ΔE_{ZPE} is the zero-point energy change and ΔS is the entropy change.

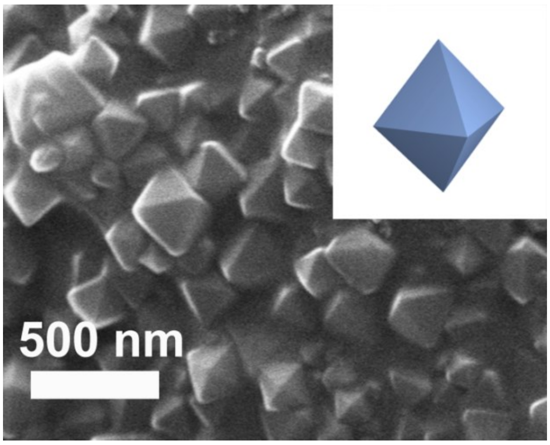

Figure S1 SEM image of UiO−66−NH$_2$

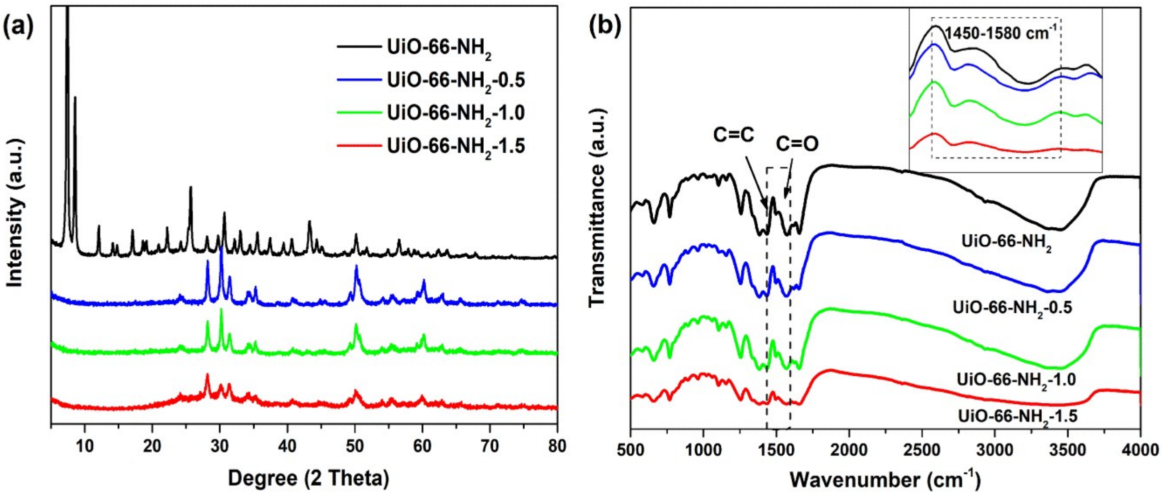

Figure S2 (a) XRD patterns and (b) FTIR spectra of Zr−MOFs with different NH_4OH content.

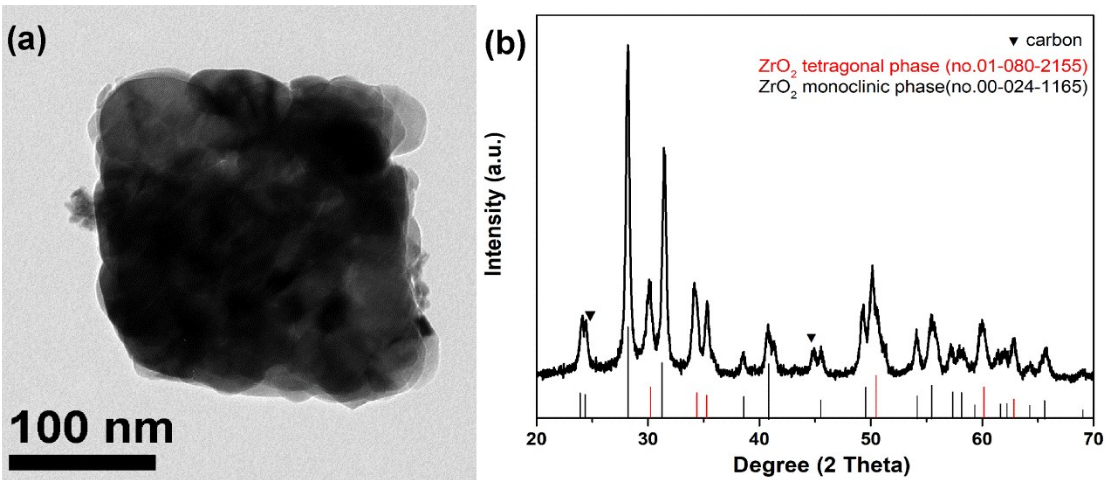

Figure S3 (a) TEM image and (b) XRD pattern of the composite without HF etching.

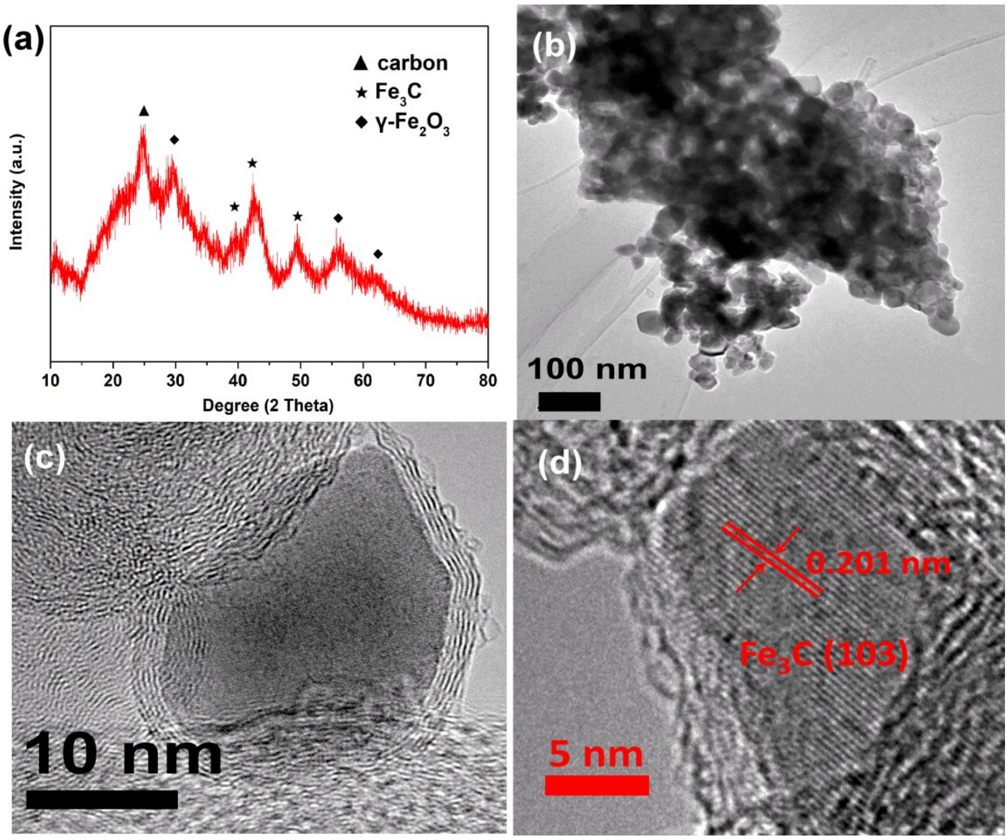

Figure S4 (a) XRD pattern and (b-d) TEM images of the Fe–N–Vulcan.

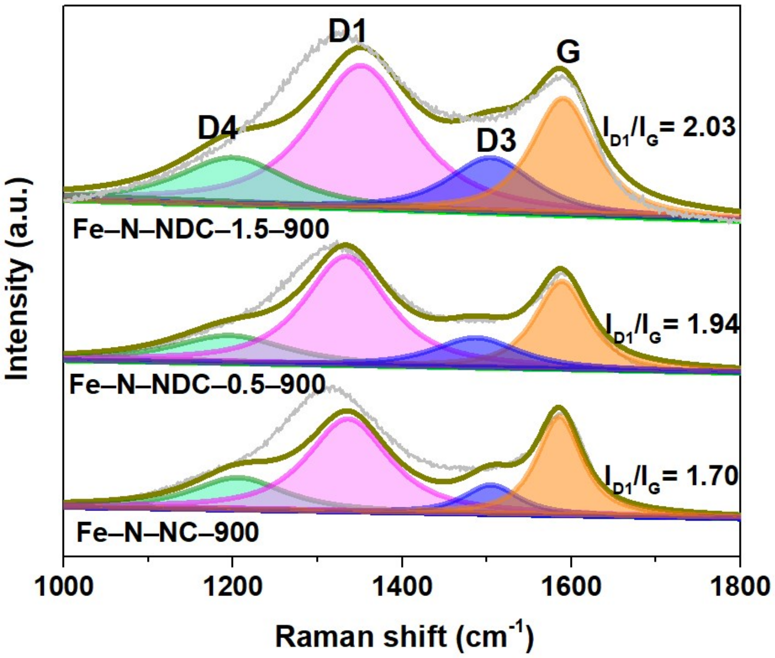

Figure S5 Raman spectra of Zr-MOFs derived Fe-N-C catalysts prepared at 900 ℃.

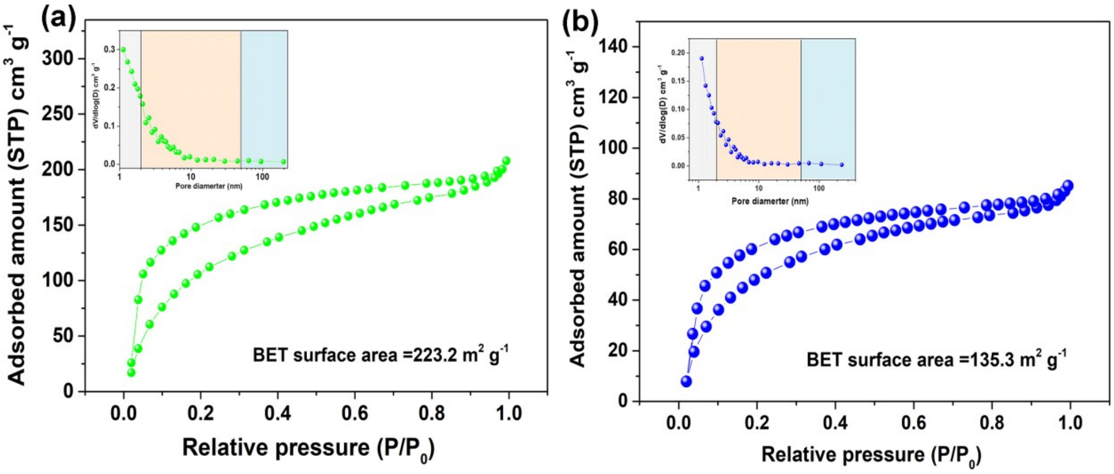

Figure S6 Nitrogen sorption isotherms of Fe–N–NDC–0.5–900 and Fe–N–NDC–1.5–900, inset is the corresponding pore distribution.

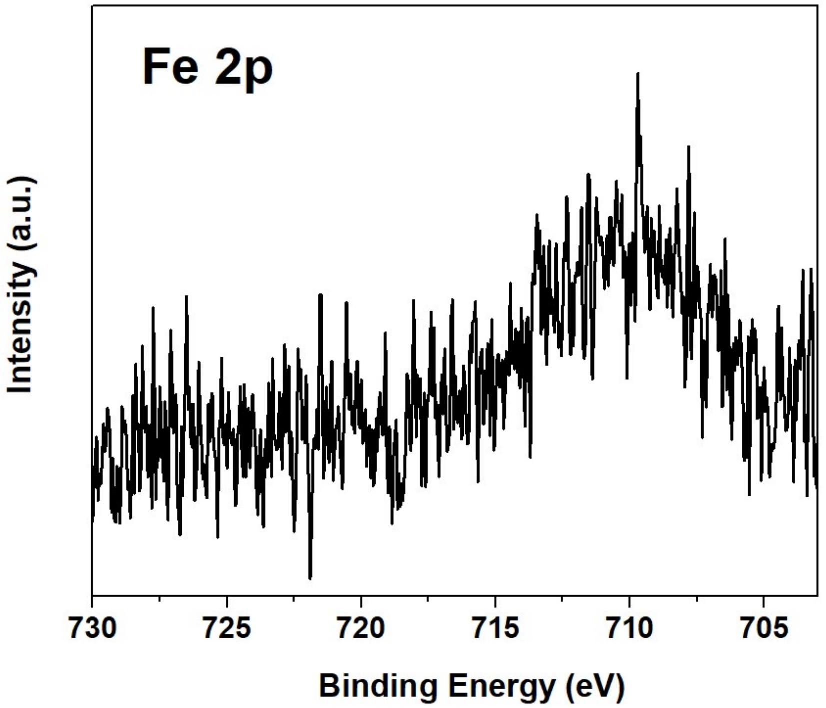

Figure S7 High resolution XPS spectra for Fe 2p in Fe–N–NDC–1–900.

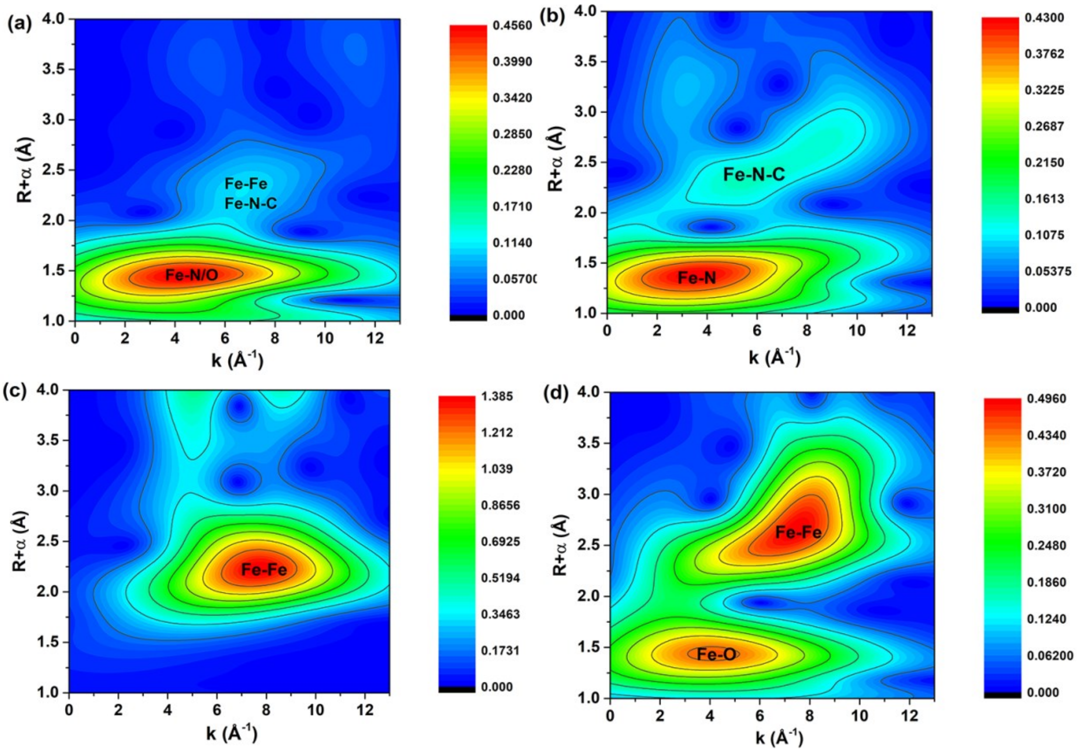

Figure S8 Wavelet transform (WT) of (a) Fe–N–NDC–1–900, (b) FePc, (c) Fe foil and (d) Fe_2O_3.

Table S1 EXAFS fitting parameters at the Fe K-edge for various samples（S_0^2=0.70）

Sample	Shell	N^a	R(Å)^b	$\sigma^2\times10^3$(Å^2)^c	ΔE_0 (eV)^d	R factor
Fe foil	Fe-Fe	8*	2.47±0.01	4.7±0.9	6.4±1.3	0.002
	Fe-Fe	6*	2.85±.01	6.0±1.7	5.1±2.6	
Fe_2O_3	Fe-O	5.6±1.2	1.98±0.02	9.5±2.9	-6.3±2.6	0.012
	Fe-Fe	6.9±1.3	3.00±0.01	9.0±1.5	1.0±1.8	
	Fe-Fe	3.6±1.2	3.66±0.02	3.2±2.0	-9.8±2.8	
FePc	Fe-N	4.3±1.4	1.99±0.02	8.2±3.4	8.9±4.4	0.014
	Fe-C	4.5±2.5	2.98±0.03	9.3±4.2	7.3±4.7	
Fe-a	Fe-N	9.4±2.0	2.01±0.02	10.9±2.5	-0.3±2.5	0.010
	Fe-C	5.3±3.2	2.94±0.04	10.7±4.3	-10.5±6.7	
Fe-b	Fe-O	5.7±1.1	1.98±0.02	9.6±2.4	-1.7±2.4	0.010
	Fe-C	4.1±2.6	2.94±0.04	11.7±4.8	-10.9±7.2	

$^a N$: coordination numbers; $^b R$: bond distance; $^c\sigma^2$: Debye-Waller factors; ^{d} ΔE_0: the inner potential correction. R factor: goodness of fit.

The obtained XAFS data was processed in Athena (version 0.9.25) for background, pre-edge line and post-edge line calibrations. Then Fourier transformed fitting was carried out in Artemis (version 0.9.25). The k^2 weighting, k-range of 2- 12 Å^{-1} and R range of 1 - ~3 Å were used for the fitting. The model of bulk Fe, FePc and Fe_2O_3

were used to calculate the simulated scattering paths. The four parameters, coordination number, bond length, Debye-Waller factor and E_0 shift (CN, R, σ^2, ΔE_0) were fitted without anyone was fixed, constrained, or correlated. For Wavelet Transform analysis, the $\chi(k)$ exported from Athena was imported into the Hama Fortran code. The parameters were listed as follow: R range, 1 - 4 Å, k range, 0 - 13 Å^{-1}; k weight, 2; and Morlet function with κ=10, σ=1 was used as the mother wavelet to provide the overall distribution.

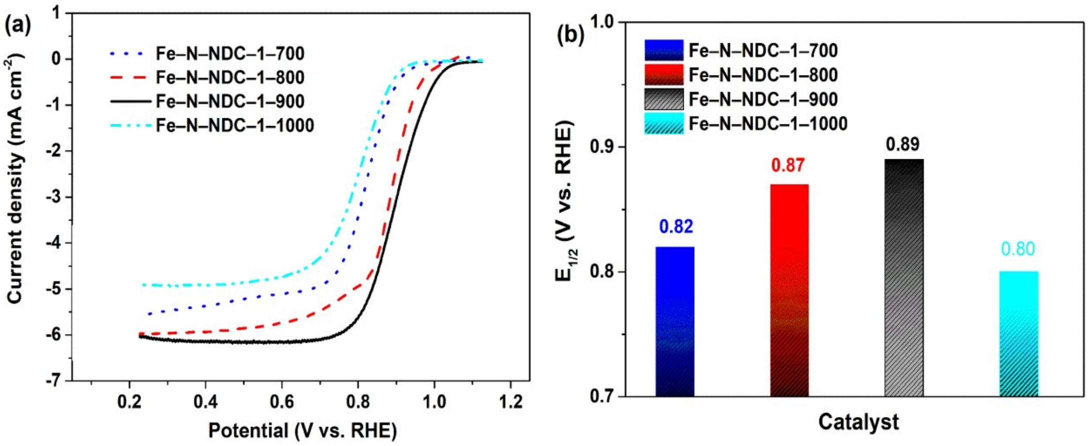

Figure S9 (a) LSV curves and (b) half–wave potentials of the Fe–N–NDC–1-T (T represents different pyrolysis temperatures).

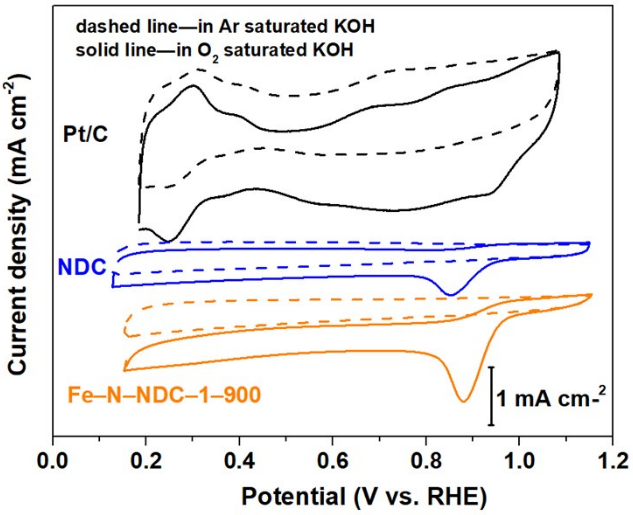

Figure S10 CV curves of Fe–N–NDC–1–900, NDC, and Pt/C on GC electrodes in O_2-saturated and Ar-saturated 0.1 M KOH.

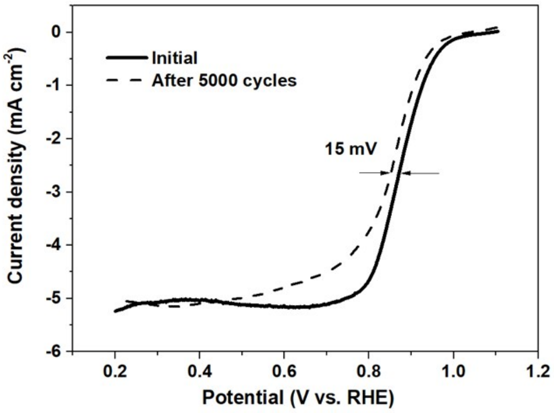

Figure S11 LSV curves of Pt/C initially and after 5000 cycles between 0.6 and 1.0 V at a scan rate of 100 mV s^{-1}.

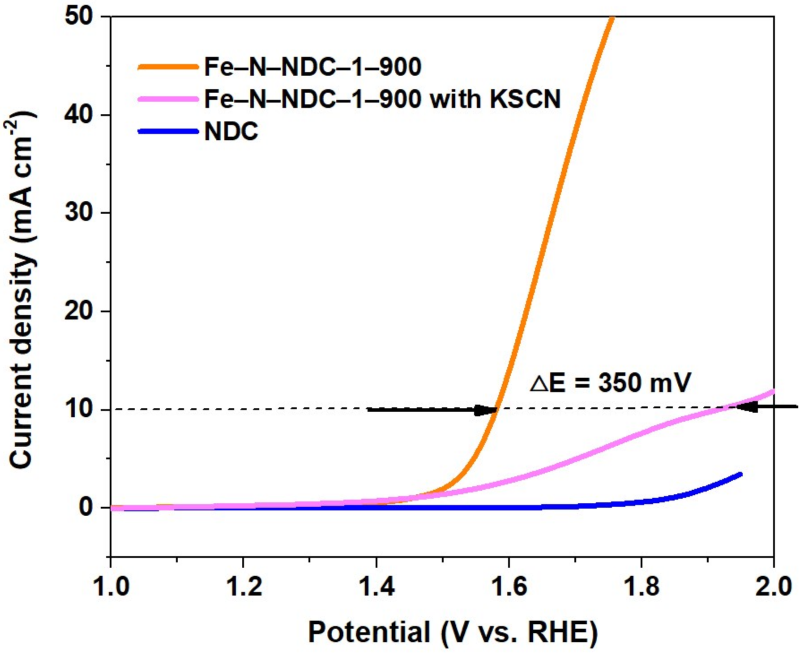

Figure S12 LSV curves of NDC, Fe–N–NDC–1–900 with and without 0.05 M KSCN in 0.1 M KOH.

Table S2 Comparison of ORR and OER activity of Fe–N–NDC–1–900 with other non-noble metal in alkaline medium

Catalyst	**E_{onset} (ORR)**	**$E_{1/2}$ (ORR)**	**E_{10} (OER)**	**ΔE (E_{10}- $E_{1/2}$)**	**Ref.**
Fe–N–NDC–1–900	1.06	0.89	1.58	0.69	**This work**
$Fe_3C/Co(Fe)O_x$@NCNT	0.97	0.86	1.58	0.72	[1]
Co_4N@NC-m	0.98	0.87	1.62	0.75	[2]
CoCe-600N_2	0.97	0.86	1.50	0.64	[3]
ZIF-9_Fe3_Pyrol	0.90	0.81	1.62	0.81	[4]
$NiIn_2S_4$/CNFs	0.91	0.81	1.62	0.81	[5]
f-CoNC/GO	NA	~0.86	1.58	0.76	[6]
CoN_4/NG	0.98	0.87	1.61	0.74	[7]
N, O-doping carbon	0.90	0.78	1.58	0.80	[8]
f-FeCo-CNT	~0.96	~0.87	1.71	0.85	[9]
Fe-NC SAC	NA	0.88	1.68	~0.80	[10]

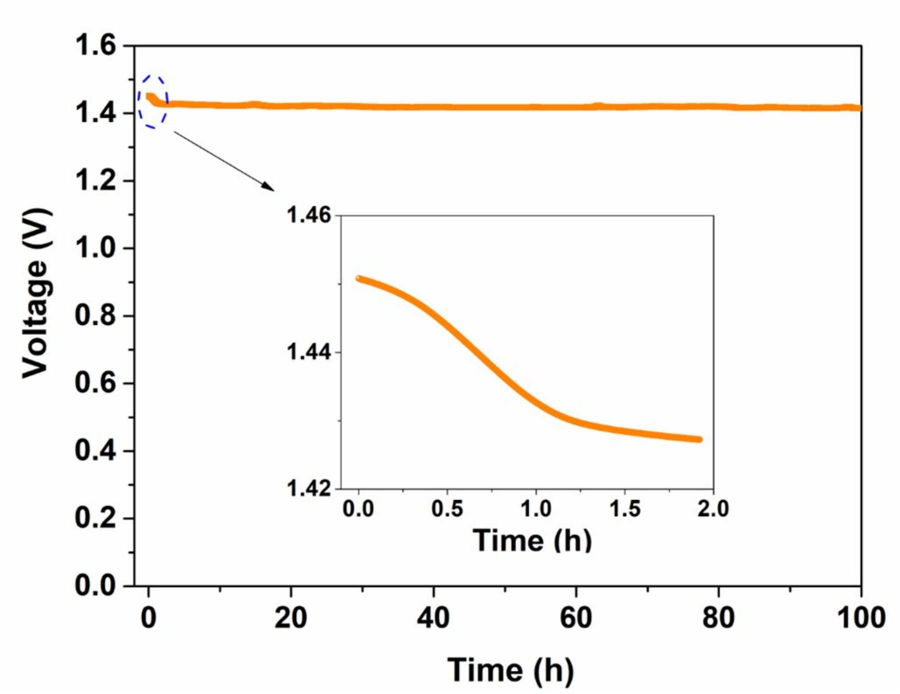

Figure S13 Discharge curve of ZAB at 1 mA cm^{-2} for 100 h using Fe–N–NDC–1–900 as air cathode.

During the charging process (oxygen evolution reaction), O_2 generates and the structure of gas diffusion layer was destroyed, which may result in the destruction of triple–phase reaction region in the electrode. Therefore, the initial discharge voltage (oxygen reduction reaction) decayed during the first two hour.

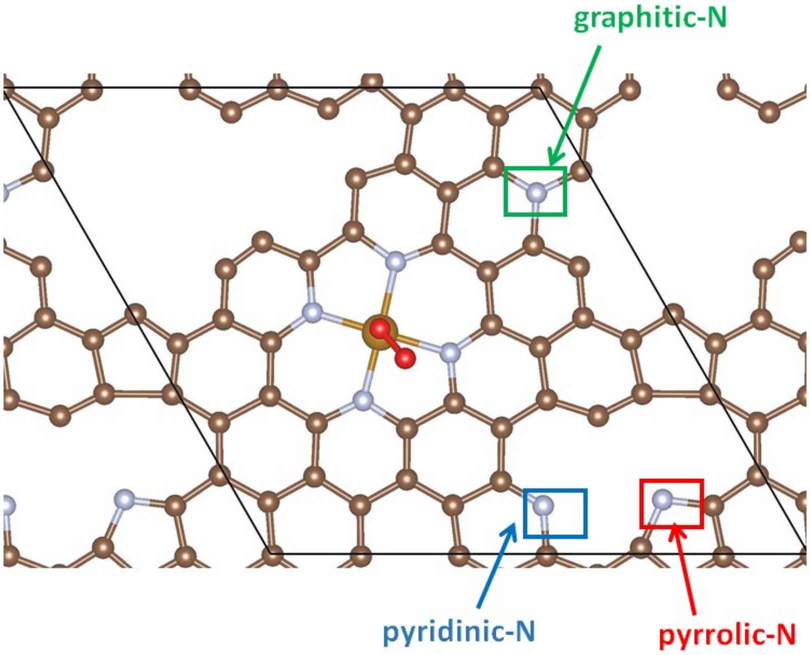

Figure S14 Schematic illustration of N configurations in Fe–N–NDC–1–900 catalyst model.

Fig. 1e and Figure S5 displayed that the Fe–N–NDC–1–900 endows the most total amount of defects ($I_{D1}/I_G = 2.14$). In addition, as shown in XPS spectra, nitrogen species in Fe–N–NDC–1–900 can be divided into pyrrolic-N, Fe-N, pyridinic-N, and graphitic-N, respectively. When constructed the model of Fe–N–NDC–1–900, N configurations were also taken into full consideration, as shown in Figure S14. And the relative content has been optimized during the modeling process.

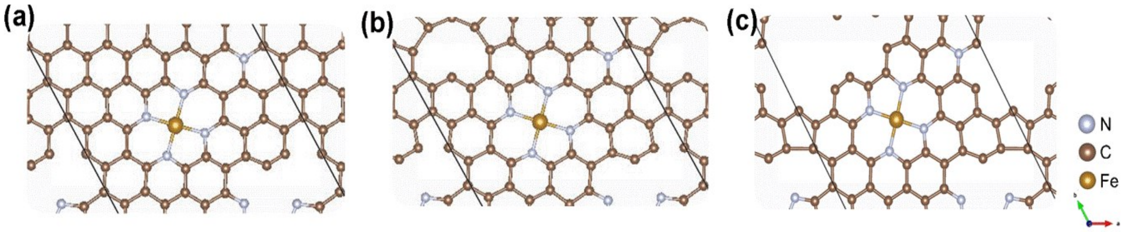

Figure S15 Schematic illustration of defective evolution for Fe–N_4 sites when varying the amount of reactant NH_4OH: (a) Fe–N–NC (without NH_4OH), (b) Fe–N–NDC–0.5–900, and (c) Fe–N–NDC–1–900.

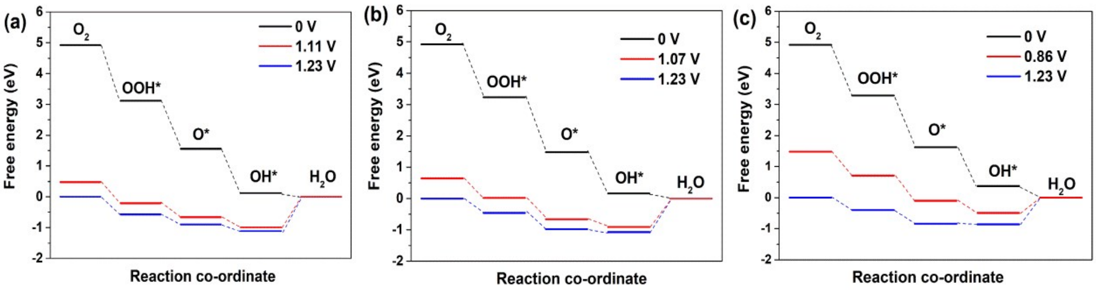

Figure S16 Free–energy paths of ORR on the Fe–N_4 site for (a) Fe–N–NC, (b) Fe–N–NDC–0.5–900 and (c) Fe–N–NDC–1–900 in an alkaline solution.

References

[1] M. Wang, T. Qian, S. Liu, J. Zhou, C. Yan, ACS applied materials & interfaces 9 (2017) 21216-21224.

[2] L. Chen, Y. Zhang, X. Liu, L. Long, S. Wang, X. Xu, M. Liu, W. Yang, J. Jia, Carbon 151 (2019) 10-17.

[3] X. He, X. Yi, F. Yin, B. Chen, G. Li, H. Yin, Journal of Materials Chemistry A 7 (2019) 6753-6765.

[4] A. Pendashteh, S.M.F. Vilela, I. Krivtsov, D. Ávila-Brande, J. Palma, P. Horcajada, R. Marcilla, Journal of Power Sources 427 (2019) 299-308.

[5] G. Fu, Y. Wang, Y. Tang, K. Zhou, J.B. Goodenough, J.-M. Lee, ACS Materials Letters 1 (2019) 123-131.

[6] Y. Jia, Y. Wang, G. Zhang, C. Zhang, K. Sun, X. Xiong, J. Liu, X. Sun, Journal of Energy Chemistry 49 (2020) 283-290.

[7] L. Yang, L. Shi, D. Wang, Y. Lv, D. Cao, Nano Energy 50 (2018) 691-698.

[8] X. Xiao, X. Li, Z. Wang, G. Yan, H. Guo, Q. Hu, L. Li, Y. Liu, J. Wang, Applied Catalysis B: Environmental 265 (2020) 118603.

[9] Y. Wang, A. Kumar, M. Ma, Y. Jia, Y. Wang, Y. Zhang, G. Zhang, X. Sun, Z. Yan, Nano Research 13 (2020) 1090-1099.

[10] C. Du, Y. Gao, J. Wang, W. Chen, Journal of Materials Chemistry A 8 (2020) 9981-9990.